NIH Public Access
Author Manuscript
Int J Radiat Oncol Biol Phys. Author manuscript; available in PMC 2007 October 31.

Published in final edited form as:
Int J Radiat Oncol Biol Phys. 2007 July 1; 68(3): 920–934.

PATIENT STUDY OF *IN VIVO* VERIFICATION OF BEAM DELIVERY AND RANGE, USING POSITRON EMISSION TOMOGRAPHY AND COMPUTED TOMOGRAPHY IMAGING AFTER PROTON THERAPY

Katia Parodi, Ph.D.[*], **Harald Paganetti, Ph.D.**[*], **Helen A. Shih, M.D.**[*], **Susan Michaud, R.T.T.**[*], **Jay S. Loeffler, M.D.**[*], **Thomas F. Delaney, M.D.**[*], **Norbert J. Liebsch, M.D.**[*], **John E. Munzenrider, M.D.**[*], **Alan J. Fischman, M.D.**[†], **Antje Knopf, M.S.**[*], and **Thomas Bortfeld, Ph.D.**[*]

[*]*Department of Radiation Oncology, Massachusetts General Hospital and Harvard Medical School, Boston, MA*

†*Division of Nuclear Medicine, Department of Radiology, Massachusetts General Hospital and Harvard Medical School, Boston, MA*

Abstract

Purpose—To investigate the feasibility and value of positron emission tomography and computed tomography (PET/CT) for treatment verification after proton radiotherapy.

Methods and Materials—This study included 9 patients with tumors in the cranial base, spine, orbit, and eye. Total doses of 1.8–3 GyE and 10 GyE (for an ocular melanoma) per fraction were delivered in 1 or 2 fields. Imaging was performed with a commercial PET/CT scanner for 30 min, starting within 20 min after treatment. The same treatment immobilization device was used during imaging for all but 2 patients. Measured PET/CT images were coregistered to the planning CT and compared with the corresponding PET expectation, obtained from CT-based Monte Carlo calculations complemented by functional information. For the ocular case, treatment position was approximately replicated, and spatial correlation was deduced from reference clips visible in both the planning radiographs and imaging CT. Here, the expected PET image was obtained from an analytical model.

Results—Good spatial correlation and quantitative agreement within 30% were found between the measured and expected activity. For head-and-neck patients, the beam range could be verified with an accuracy of 1–2 mm in well-coregistered bony structures. Low spine and eye sites indicated the need for better fixation and coregistration methods. An analysis of activity decay revealed as tissue-effective half-lives of 800–1,150 s.

Conclusions—This study demonstrates the feasibility of postradiation PET/CT for *in vivo* treatment verification. It also indicates some technological and methodological improvements needed for optimal clinical application.

Keywords

Proton therapy; PET/CT; Monte Carlo

Reprint requests to: Katia Parodi, Ph.D., now at the Heidelberg Ion Therapy Center, Im Neuenheimer Feld 450, 69120 Heidelberg, Germany. Tel: (+49) 62215638239; Fax: (+49) 62215687392; E-mail: Katia.Parodi@med.uni-heidelberg.de

Conflict of interest: none.

NIH-PA Author Manuscript
NIH-PA Author Manuscript
NIH-PA Author Manuscript

NIH-PA Author Manuscript

NIH-PA Author Manuscript

NIH-PA Author Manuscript

INTRODUCTION

Compared to conventional external radiation treatment modalities, proton beams allow a more conformal dose deposition to the tumor, with better sparing of surrounding critical structures and normal tissue. Modern delivery techniques and planning strategies, such as beam scanning and intensity modulation, may enable optimal utilization of this advantage. However, full clinical exploitation of proton-beam precision is hampered by uncertainties in the localization of the distal dose fall-off within the patient. Proton treatment-planning strategies often only utilize the lateral penumbra of the beam in the proximity of critical organs for dose conformation. Of concern are dose-calculation errors of simplified pencil-beam algorithms, and the use of empiric calibration curves between computed tomography (CT) numbers and proton range, especially in the presence of tissue heterogeneities and metallic implants. Furthermore, proton therapy is more sensitive to standard sources of uncertainties such as beam-delivery or patient-setup errors and organ motion. Although the use of margins in treatment planning safely accounts for uncertainties, *in vivo* verification of a treatment and, in particular, of the proton range in a patient would be beneficial, and this could potentially reduce margins and improve conformality.

Positron emitters such as ^{11}C and ^{15}O are produced via nuclear interactions along the proton-beam path, and can be imaged during (online) or shortly after (offline) treatment as a spatial marker of radiation-dose deposition. Previous offline and online phantom experiments indicated the sufficient accuracy of positron emission tomography (PET) imaging for the verification of proton range and field lateral position [(1,2) and citations therein]. Based on experience in clinical routine applications of in-beam PET to carbon ion treatment verification (3), a similar potential was discussed for proton beams, despite their limitation in β^+-activation of target fragments (2). Positron emission tomography scans taken 3–5 min after one proton treatment fraction of 2 patients with a larynx (4) and an ethmoid sinus carcinoma (5) tumor envisaged clinical feasibility. However, both studies were limited to a qualitative visual comparison between the planned dose distribution and its corresponding measured PET image, which is not directly proportional to the pattern of energy deposition. The present work follows a detailed, preclinical phantom study (6), and aims at a more systematic and quantitative investigation of the clinical feasibility and value of the recently integrated PET/CT imaging modality. Our main goal was to address the possibility of *in vivo* verification of proton range. This study also provides insights into the human metabolism of radiation-induced β^+-activation.

METHODS AND MATERIALS

Nine patients walked to the PET/CT scanner immediately after completion of one treatment session during the course of fractionated proton radiation therapy. Their PET/CT data were acquired and reconstructed according to a protocol specifically designed for this study. Images were rigidly coregistered to the planning CT or radiopaque clip positions (in the case of an ocular melanoma) for comparison with the planned dose and its corresponding PET expectation. The latter was obtained from a CT-based Monte Carlo (MC) calculation or a recently proposed analytical model (in the ocular case), both complemented by functional information.

Subject selection and treatment

After approval of the investigational protocol by our Investigational Review Board, potential subjects receiving fractionated proton radiation at Massachusetts General Hospital (Boston, MA) received the opportunity to participate in this study. In total, 9 subjects were enrolled. They were 6 males and 3 females, with mean and median ages of 43.8 and 49 years, respectively

NIH-PA Author Manuscript

NIH-PA Author Manuscript

NIH-PA Author Manuscript

(range, 25–62 years). All subjects had a Karnofsky performance status of ≥80, and were able to ambulate without difficulty or assistance.

Tumor types included chordoma (3), chondrosarcoma (2), malignant peripheral nerve-sheath tumor, primitive neuroectodermal tumor, ocular melanoma, and pituitary macroadenoma. Anatomic sites irradiated included the clivus (2), spine (4), sella, orbit, and ocular globe. Target treatment doses ranged from 50–77.4 GyE, with a dose per fraction range of 1.8–10 GyE delivered in 1–2 fields. Most subjects received between 1.8–2 GyE per fraction, with the exception of 3 GyE for a recurrent and metastatic chordoma, and 10 GyE for an ocular melanoma treated in a daily hypofractionated course to 50 GyE. Irradiation was performed in gantry-equipped treatment rooms for all patients except for the one with ocular melanoma, who was treated on a fixed eye beam line.

Imaging protocol

PET/CT acquisition—Imaging was performed at a commercial PET/CT scanner (Biograph Sensation 16, CTI/Siemens, Knox-ville, TN), using state-of-the-art (at the expense of minor intrinsic radioactivity) PET detectors based on lutetium oxyorthosilicate (LSO). The scanner is located in the Department of Radiology of Massachusetts General Hospital. All patients were able to proceed from the proton unit to the imaging site within 10 min immediately after their treatment. Learning from an unsuccessful attempt to avoid fixation for the sake of patient comfort, treatment position was replicated for 7 patients using the same treatment immobilization device. Rigid fixation in supine position for cranial-base tumors was obtained from commercial, individually shaped thermoplastic masks (Tru-Scan Imaging, Annapolis, MD), complemented by a custom, in-house-designed, carbon-fiber support for cervicothoracic tumors. For the lower-spine sites, a commercial, nonrigid immobilization device was used, consisting of a resting frame for the head, and handles for the arms of the patient in prone position (Red-Care Products, Sunnyvale, CA). Details on immobilization accuracy and reproducibility can be found elsewhere (7). For the patient with an ocular melanoma, exact replication of treatment position under eyelid retraction and visual fixation on a flashing light was judged unfeasible because of a risk of corneal injury and patient discomfort. The patient was scanned in supine position, with only approximately replicated eye orientation based on recall.

The initial CT served for localization of the anatomic region of interest for the emission scan, as well as for the determination of the attenuation correction map. Subsequent PET acquisition was performed in list mode for 30 min, starting within 13–20 min after the end of irradiation. Only one bed position was employed, despite insufficient axial coverage (≤16.2 cm) for three large spine tumors. The reason for this involved the extremely low counting statistics (10^2–10^3 counts per second [cps]) for this unconventional PET application. The mandatory input information for the imaged radiotracer was set to ^{22}Na (half-life [$T_{1/2}$] = 2.6 years), to eliminate any decay correction. Quantification of activity from the mixed β^+-emitting source induced by proton irradiation was corrected for the ^{22}Na branching ratio.

Image reconstruction—Computed-tomography images were reconstructed on a voxel grid of 0.5–1 mm transaxial pixel size (depending on anatomic location) and 3 mm axial thickness, *i.e.*, comparable to the planning CT dimensions for optimal rigid coregistration. The latter was performed via commercial FOCAL software (Computerized Medical Systems, Inc., St. Louis, MO), using mutual information maximization. In the ocular case, the CT slice thickness was reduced to 1 mm for better localization of the radiopaque clips.

The PET images were reconstructed with a transaxial pixel size of about 1.3 mm and a fixed slice thickness of 3.375 mm. The integral distribution of activity was obtained from filtered back-projection (FBP) and iterative (ordered subsets expectation maximization; OSEM)

NIH-PA Author Manuscript

NIH-PA Author Manuscript

NIH-PA Author Manuscript

reconstruction of all measured data (6). The OSEM was preferred because of reduced fluctuations, especially in the low-activity region at the edge of the field of interest for range verification. Dynamic studies were performed using FBP, yielding more accurate quantification for decay analysis. As a good compromise between short frame duration and reasonable counting statistics, the 30 min of acquisition were reconstructed in 20 frames of 1 min, followed by 5 frames, each 2 min long.

Calculation model

Expected PET images were obtained from the calculation of (*1*) the spatial distribution of positron emitters produced in the patient, corrected with space- and time-dependent weighting factors accounting for (*2*) biologic decay and (*3*) image formation.

Positron emitter distributions—For all patients except for the case of ocular melanoma, irradiation-induced positron emitter distributions were obtained from MC calculations on the radiation-planning CT. Particle transport within the patient was performed using the FLUKA code (8), starting from the initial (in air) beam phase-space obtained from MC simulation of the gantry treatment head with patient-specific beam modifiers (9). Conversion of Hounsfield units (HU) into mass density and elemental composition was based on a segmentation of the CT scan into 26 materials sharing the same composition and a nominal mean density for $-1{,}000 \leq \text{HU} < 3{,}060$ (6,10,11), and into titanium for HU $\geq 3{,}060$ (6). The HU-dependent adjustment of electromagnetic and nuclear processes within each material was accomplished using scaling factors to reproduce the calibration curve used by the treatment-planning (TP) dose algorithm, and to account for differences between real and nominal density (6,10). Positron emitter distributions were calculated by internally combining proton fluence with experimental cross sections (12). Besides the main (*p*, *pn*) channels on ^{12}C and ^{16}O yielding ^{11}C and ^{15}O (12), respectively, further proton interactions with N, O, Ca, and P, resulting in ^{11}C, ^{13}N, ^{38}K, and ^{30}P production, respectively, were included. Shorter-lived emitters were neglected because of the low-production cross-section and the offline PET imaging approach. Dose, *i.e.*, energy deposition per volume divided by the real (not nominal) density, was additionally calculated for comparison with the treatment plan. In this way, the correspondence between measured and MC-simulated PET images can provide a true feedback on the delivery of the intended (planned) dose, separating possible effects coming from the different MC and treatment-planning dose algorithms. A total of 3×10^6–7×10^7 primary protons were simulated, typically in 10 independent runs of about 3% (PET) and 5% (dose) statistical uncertainty. For normalization, an additional FLUKA simulation with the same input phase-space was performed in the water tank used for quality-assurance dosimetry. The normalization factor $n \approx (1\text{-}7) \times 10^3$ was given by the ratio of the prescribed to the simulated dose to water at isocenter.

In the patient with ocular melanoma, no planning CT or phase-space generation for the eye beam line was available for MC calculation. However, the simple geometry of the problem made it an ideal candidate for a recently proposed analytical model (13), in which the PET signal was deduced from the planned dose distribution. The latter was coregistered to the imaging CT, based on matching of the radiopaque clips positions. Only the expected dominant contribution of ^{11}C, produced in proton interaction on C and O, was considered (13). Because of a lack of information, the composition in C and O of the eye was approximated to the averaged soft-tissue values of 14.3% and 70.8%, respectively (14). Values from the CT calibration of Schneider *et al.* (11) were used for the remaining tissues, without attempting to correct for the metallic-implant composition. Since the planned dose distribution was used, the normalization factor *n* was unity.

NIH-PA Author Manuscript

NIH-PA Author Manuscript

NIH-PA Author Manuscript

Biologic decay—The metabolism of positron emitters induced by irradiation in living tissue is a complex process because of their unknown molecular form. This prohibits the application of compartment models, which are well-established in conventional tracer imaging. Previous animal studies on the washout of ^{10}C and ^{11}C implanted ions or ^{11}C resulting from autoactivation of ^{12}C beams indicated the existence of a fast (biologic half-life [$T_{1/2,biof}$] ≈(2–10 s), medium ($T_{1/2,biom}$ ≈100–200 s), and slow ($T_{1/2,bios}$ ≈ 3,000–10,000 s) component of biologic decay in rabbit thigh muscle and brain (15,16). In our offline imaging approach, the fast and medium processes have already decayed at the time of imaging. Following the mathematical formulation of Mizuno *et al*. (16), the slow biologic effect was introduced as a space- (*i.e.*, tissue) and time-dependent weighting factor $C_{bios}(\boldsymbol{r}, t) = M_s(\boldsymbol{r})\exp(-\lambda_{bios}(\boldsymbol{r})\, t)$ of the physical activity. Values of the relative fraction M_s, and biologic decay constant $\lambda_{bios}(\lambda_{bios} = \log_e 2/T_{1/2,bios})$ are, however, unknown for the various isotopes in human tissues. For the sake of simplicity, we classify tissue into low, intermediate, and normal perfusion, and neglect differences between the metabolisms of different isotopes. Thresholds were set on the planning CT to identify fat ($-150 \le HU \le -30$), soft bone ($200 \le HU < 1{,}000$) and compact bone ($HU \ge 1{,}000$). For the low-perfusion fat and compact bone, M_s and $T_{1/2,bios}$ were set to 0.9 and 15,000 s, respectively. In soft bone, intermediate values of M_s and $T_{1/2,bios}$ were approximated to 0.6 and 8,000 s. For all remaining tissue, an average value of $M_s = 0.55$ and $T_{1/2,bios} = 3{,}500$ s was used in spine sites, while a value of $M_s = 0.35$ and $T_{1/2,bios} = 10{,}000$ s was used for head sites, based on the results of animal studies in muscle and brain, respectively (16). In the patient with ocular melanoma, reduced perfusion ($M_s = 0.8$, $T_{1/2,bios} = 10{,}000$ s) was assumed within the eye, whereas an average value of 0.45 (M_s) and 6,000 s ($T_{1/2,bios}$) was used for the surrounding tissue.

PET images

For the full-ring tomograph, blurring from image formation and reconstruction can be reasonably modeled by a three-dimensional (3D) Gaussian convolution kernel $G(\mathbf{r})$, as supported by a previous phantom study (6). Neglecting the slow biologic decay during the short irradiation time ($t_{irr,i} \approx 10$–100 s), a PET image, averaged on a time frame of duration t_{frame} starting with a time delay Δt after the end of irradiation, was obtained from the sum of activity contributions from the calculated amount N_{ij} of isotopes of species j, formed by each delivered field i:

$$G(\mathbf{r}) * \left\{ \sum_i n_i \cdot \sum_j \left[M_s(\mathbf{r}) N_{ij}(\mathrm{r}) \cdot \frac{[1 - \exp(-\lambda_j t_{irr,i})]}{t_{irr,i}} \cdot \exp(-\lambda_{tot,j}(\mathbf{r})\Delta t) \cdot \frac{[1 - \exp(-\lambda_{tot,j}(\mathbf{r}) t_{frame})]}{\lambda_{tot,j}(\mathbf{r}) t_{frame}} \right] \right\}$$

where n_i is the normalization factor for the considered field, M_s is the slow biologic decay fraction, and λ_j and $\lambda_{tot,j}$ are the isotope-specific physical and total (*i.e.*, physical plus biologic) decay constants, respectively.

Data analysis

For analysis in the space domain, a MATLAB (MathWorks, Inc., Natick, MA)-based code was developed to compare planned and MC-simulated dose distributions as well as measured and calculated PET/CT images, all superimposed or coregistered to the planning CT. In the patient with ocular melanoma, PET and dose data were coregistered to the only available imaging CT. The profiles shown below (averaged over ±2–3 mm) compare absolute (*i.e.*, not normalized) values. Information on proton range and lateral field position is extracted from the distal 50% (30% in the ocular case) fall-off position. The 2D images are shown in color-wash display, normalized to the local maximum within the selected axial, coronal, or sagittal slice. Values below a threshold of 8% of the maximum were omitted for visual reduction of the noise of the measured PET images.

NIH-PA Author Manuscript

NIH-PA Author Manuscript

NIH-PA Author Manuscript

In the time domain, the decay of measured and calculated activity was studied for different patients in selected regions of interest (ROIs). Tissue was classified based on visual anatomic evaluation and HU values (mean ± SD) of the corresponding ROIs in both CTs from the PET/CT and planning CT scanner. Effective half-lives were determined by weighted nonlinear least-squares fitting of decay curves, with a single exponential function.

RESULTS

Irradiation-induced β^+-activation could be visualized using the commercial PET/CT scanner for all patients, despite the long delay between treatment and imaging as well as the intrinsic radioactivity of the LSO-based detectors, yielding a background comparable to the signal (6).

Spatial distributions

Cranial base—Figures 1-3 show axial views and one sagittal view of planned as well as MC-calculated dose distributions and corresponding simulated PET/CT images against measurements for cases of cranial-base tumors. Activation from all delivered fields is visible in the PET images, with stronger intensity from the last portal. For the patient with a pituitary tumor (Fig. 1) and for all posterior–anterior fields, most of the activity formed in the brain was washed out, resulting in a local-activity maximum in the entrance fat and bone as well as in the distal tumor. This is evident when comparing the MC results before and after correction for biologic decay (Fig. 4). Posterior–anterior irradiation also clearly activated the brainstem white matter, which has a higher composition in carbon (19.4%) than in the surrounding gray matter (9.5%) and cerebrospinal fluid (0%) (11). This brainstem activation seen in the measurement is not reproduced by the MC because of the difficulty to differentiate brain tissue using blind CT windowing. Instead, activation throughout almost the whole penetration depth along the base of the skull is visible for the lateral portals of the 2 patients with clival tumors (Figs. 2, 3).

In terms of range verification, examples of depth profiles for the orthogonal fields of Figs. 1 and 2 are shown in Fig. 5, and are analyzed in Table 1. Larger differences between the TP and MC dose are found for posterior–anterior fields in air, similar to the findings of Jiang and Paganetti (10). In tissue, 50% and 80% dose fall-offs agree within 0.2–1.8 mm. Corresponding positions of the measured and simulated-activity distal maximum and 50% fall-off agree within 0.6–1.9 mm. The 50% activation fall-off is 8–18 mm before the corresponding dose fall-off. The larger separations occur for particles stopped in perfused soft tissue (lateral field of Fig. 1) or in air cavities (posterior–anterior fields), where no material is activated but where the deposited dose is not of clinical significance.

Spine—The spine sites differed in terms of immobilization accuracy and PET signal attenuation. Figure 6 shows images for the rigidly immobilized patient with a cervicothoracic tumor. The activation track is still visible for both portals, despite the low dose and long-delay ΔT for the first posterior–anterior field. Again, the local-activity maxima in fat and bone are due to a high concentration in carbon (and calcium in bone) and low biologic clearance. The PET measurement shows a higher activation of the carbon-fiber frame, which is not well-reproduced by the calculation using CT calibrations based on real-tissue data. Despite the imperfect coregistration in the shoulder region, agreement of 1–3 mm is found for the 50% fall-off position of measured and calculated PET profiles in the distal, well-coregistered bony region. Similar agreement within 0.2–2 mm was observed for the TP and MC 80% and 50% dose fall-offs. Because of the field overlap and limited bone perfusion, the latter 50% dose fall-off can be found down to 1 mm beyond the corresponding PET fall-off.

Figure 7 shows a lumbar-spine patient with titanium implants. In this case, planned and MC dose distributions exhibit differences in the region of the metallic implants and related CT

NIH-PA Author Manuscript

NIH-PA Author Manuscript

NIH-PA Author Manuscript

artifacts, making *in vivo* verification highly beneficial. In general, the distal shape of measured and predicted activity confirms the sparing of critical structures such as the kidneys. However, the data shown do not allow accurate range verification in the critical region affected by the implants and artifacts. Clear limitations arise from the rigid coregistration, *e.g.*, missing the abdominal expansion caused by the different shape of the PET/CT and planning CT scanner tables, in combination with respiratory-motion uncertainties. Moreover, the image quality for the low-intensity activity distal edge deep inside the patient is considerably degraded because of the large object size, corresponding to a 91% average attenuation, against 78% for the cervico-thoracic and 81–83% for the head sites. Still, validation of the lateral-field position can be obtained from the highly activated entrance fat layer beneath the skin, common to all imaged patients. Positron emission tomography provides "portal-imaging-like" information, reproducing the shape of the collimator. The lateral measured activity distribution agrees within 2 mm with the PET calculation and the planned as well as the MC dose (Fig. 8). Similar findings apply to the sacral patient, although range agreement up to 1–2 mm could be found for protons stopped in the better-coregistered lumbar spine above the sacral region (Fig. 9).

Orbit and eye—While the considered recurrent chordoma in the orbit presented many analogies with the cranial-base sites, the case of choroidal melanoma is peculiar because of the small (0.23 cm^3) tumor size, high fraction dose, positioning issues, and different strategies for treatment-planning and PET calculations. Figure 10 shows dose and corresponding PET calculations and measurements coregistered to the PET/CT. The lateral position of the measured local-activity maximum in the eye is well-reproduced by the calculation (Fig. 10, left). However, correct alignment of the eye-gazing angle, based on the matching of fiducial markers, is problematic because of limited CT accuracy in the presence of artifacts from metallic implants (Fig. 10, right). Measured and calculated depth profiles traversing the most posterior part close to the implants, *i.e.*, less subject to position uncertainty, agree within 0.2–3.4 mm in the more distal fall-off, *e.g.*, the 30% level located about 10 mm before the corresponding dose drop (Fig. 11). Dynamic reconstructions confirmed reduced distal variation (≤1–2 mm), in part because of motion blurring, in this posterior part. Data taken in the first 10 min of acquisition offer a reasonable signal-to-noise ratio and reduced smearing from patient movement. However, for this particular site, the imaged extension of the small activated area shows a dependence on the reconstruction algorithm used, demanding more careful modeling in the future, in view of range verification.

Time analysis

Measured and calculated decay curves from ROIs set in different tissues for a cranial-base and a spine patient are shown in Fig. 12. Quantitative agreement is within 30%, whereas fitted half-lives differ by 2–25%, which is within the fitting-parameter uncertainties of the noisy measured data. To better address the tissue dependence of biologic decay, normalized decay curves taken in the same tissue type for different patients were summed up to reduce statistical fluctuations. The measured data shown in Fig. 13 have average uncertainties (standard deviation to mean ratio) of 10%, 25%, 35%, 60%, and 130% in fat, soft bone, hard bone, muscle, and brain, respectively. Fitted effective half-lives are summarized in Table 2. Despite the still large uncertainties of the experimental data, a common trend is apparent. Because our offline imaging approach is mainly sensitive to ^{11}C (physical half-life [$T_{1/2}$] = 1,222.8 s), the measured effective half-lives indicate reduced biologic decay in bone and fat. Instead, increased perfusion is found in muscle and brain. These, however, exhibit the largest experimental uncertainties and the biggest deviations from the calculation, based on data from the literature on the biologic parameters of corresponding animal tissues. For the patient with ocular melanoma, an experimental effective half-life of about 1,030 s (±28%) was found in the vitreous fluid (HU = 18 ± 28), supporting the two assumptions of dominant activation from ^{11}C and limited perfusion. Increased perfusion, consistent with higher vascularization, was found for the local-

NIH-PA Author Manuscript

NIH-PA Author Manuscript

NIH-PA Author Manuscript

activity maximum in the outer eye region (HU = 54 ± 29), which shows a reduced effective half-life of about 900 s (±22%). However, the difference is on the same order of the experimental uncertainty. Quantitatively, the local-activity maximum within the eye was overestimated by about 30% by the calculation.

DISCUSSION

This study demonstrates the feasibility of imaging β^+-activation induced by proton irradiation in all considered sites at the typical fraction doses by using a commercial offline PET/CT scanner. For range monitoring, an average deviation of (−0.1 ± 2.0) mm was found between 54 measured and calculated PET profiles randomly selected in well-coregistered bony structures for tumors in the head and neck. This suggests that, in cases with reproducible rigid immobilization and low perfusion, the same level of accuracy can be achieved as in our previous phantom study (6). Larger deviations occur for low spine and ocular sites. In the former case, major limitations come from nonrigid fixation and motion uncertainties during the prolonged scan time, calling for better fixation and deformable registration. The larger object sizes also considerably degrade the image quality because of increased photon attenuation and scattering. Improved reconstruction techniques, *e.g.*, exploiting time-of-flight information (17), might be beneficial. For the patient with ocular melanoma, PET images reconstructed from the initial 10-min measurement suggest the possibility of shortening the acquisition time without compromising image quality, because of the high fraction dose and small target volume. This might enable exact replication of treatment position, which has been avoided so far because of patient discomfort and the risk of corneal injury.

Computer tomography-based MC calculations of the dose delivery and its related PET image generally corresponded well to the treatment-plan dose and the measured PET distribution, respectively. Overall, deviations of 1–5% were found between analytical and MC dose calculations (Table 1). This was caused by uncertainties in the normalization used to scale the output factor for both calculations, and by the difference between dose to water (planning system) and dose to tissue (MC). Local deviations of ≤10% can be found, especially in bony structures. Remarkable differences in the spatial distributions were observed only in the presence of metallic implants.

Use of the literature and of newly proposed data for the extraction of tissue physical and biologic parameters from CT values, in combination with experimental cross sections for positron emitter production, yielded an average quantitative agreement of 5–30% between calculated and measured PET distributions in the space and time domains. This is within the statistical uncertainties of the measured data. However, the calculation model missed details such as activation of the brainstem and of the carbon-fiber support in the cranial-base and cervico-thoracic patients. Similar discrepancies were observed in some cases in the tumor area, which behaved differently from the healthy tissue from data in the literature. Future strategies might use (planning) contour information for a more correct assignment of elemental composition and biologic parameters (when known). While not important for spatial confirmation of the delivered fields in all considered examples, accurate quantification is mandatory when attempting to extract dose information from the PET distribution. This ultimate, challenging goal can benefit from the alternative calculation model of Parodi and Bortfeld (13), as applied here for the first time to a patient with ocular melanoma.

The long time interval between irradiation and imaging prevented the acquisition of the dominant (≈10 times larger at end of irradiation) activity contribution from ^{15}O ($T_{1/2}$ = 121.8 s), which might offer the very appealing possibility of addressing tumor hypoxia and treatment response. However, clinical, online PET data are lacking for proton therapy, where the limitation to target fragmentation represents a major difference with respect to the in-beam

NIH-PA Author Manuscript

NIH-PA Author Manuscript

NIH-PA Author Manuscript

PET of carbon-ion therapy (2,3). Proton-induced activity is more sensitive to tissue elemental composition and metabolism. Even minor target fragmentation reaction channels may considerably affect the PET signal, depending on the irradiation and acquisition time courses (2). These sources of uncertainty are reduced in the considered offline scenario, due to the small number of production channels yielding long-lived positron emitters and the limitation to slow biologic processes. Although the latter implies lower signal intensity and a potentially larger distortion of the initially formed activity pattern, the clinical advantage of online vs. offline PET imaging is still questionable. Certainly, a PET/CT device is preferable to PET alone for offline imaging. The additional CT information may enable accurate coregistration between the imaging and planned treatment positions, with the advantage of exploring simultaneously the possibility of anatomic modifications with respect to the planning CT during fractionated radiotherapy.

CONCLUSIONS

Positron emission tomography and CT imaging promptly following proton therapy may offer a simple means of noninvasive, *in vivo* verification of the delivered treatment. A physical and biologic calculation model of the induced activity is needed because of the complex correlation between planned dose and measured PET. Two implementations have been presented. The strengths and weakness of the technique were analyzed for different anatomic locations. Following our encouraging results, a larger study is underway to improve performances in identified critical sites, and to explore applicability in other indications. The ultimate clinical goal for eligible sites is (*1*) to improve confidence in the planning of complex cases, *e.g.*, in the presence of large density gradients or metallic implants, and (*2*) to enable adaptive strategies in case of discrepancies between planned and actual treatment.

Acknowledgements

From the Department of Radiation Oncology (Massachusetts General Hospital, Boston, MA), we thank Alexei Trofimov, Sashi Kollipara, Skip Rosenthal, and the treatment planners for support with the planning patient data and rigid coregistration tools, John Collier for help with the eye-patient data, and Janet Sisterson for providing nuclear cross-sectional data. From the Department of Radiology (Massachusetts General Hospital, Boston, MA), we thank Nathaniel Alpert, Ali Bonab, and the technical staff for support in designing the imaging protocol and operation of the PET/CT scanner. We thank Alfredo Ferrari and Florian Sommerer from CERN (Geneva, Switzerland) for developing and providing the experimental version of the FLUKA code.

This work was supported by National Cancer Institute (NCI) Grant 5 P01 CA21239-25 for Proton Radiation Therapy Research.

References

1. Nishio T, Sato T, Kitamura H, et al. Distributions of β^+ decayed nuclei generated in the CH_2 and H_2O targets by target nuclear fragment reaction using therapeutic MONO and SOBP proton beam. Med Phys 2005;32:1070–1082. [PubMed: 15895592]
2. Parodi K, Pönisch F, Enghardt W. Experimental study on the feasibility of in-beam PET for accurate monitoring of proton therapy. IEEE Trans Nucl Sci 2005;52:778–786.
3. Enghardt W, Crespo P, Fiedler F, et al. Charged hadron tumour therapy monitoring by means of PET. Nucl Instrum Methods A 2004;525:284–288.
4. Vynckier S, Derreumaux S, Richard F, et al. Is it possible to verify directly a proton-treatment plan using positron emission tomography? Radiother Oncol 1993;26:275–277. [PubMed: 8391156]
5. Hishikawa Y, Kagawa K, Murakami M, et al. Usefulness of positron-emission tomographic images after proton therapy. Int J Radiat Oncol Biol Phys 2002;53:1388–1391. [PubMed: 12128141]
6. Parodi K, Paganetti H, Cascio E, et al. PET/CT imaging for treatment verification after proton therapy —a study with plastic phantoms and metallic implants. Med Phys 2007;34:419–435. [PubMed: 17388158]

NIH-PA Author Manuscript

NIH-PA Author Manuscript

NIH-PA Author Manuscript

7. Engelsman M, Rosenthal SJ, Michaud SL, et al. Intra- and interfractional patient motion for a variety of immobilization devices. Med Phys 2005;32:3468–3474. [PubMed: 16372417]
8. Ferrari A, Sala PR, Fassò A, *et al*. FLUKA: A multi-particle transport code, 2005; CERN 2005–10; INFN/TC[lowem]05/11; SLAC-R-773.
9. Paganetti H, Jiang H, Lee S-Y, et al. Accurate Monte Carlo simulations for nozzle design, commissioning and quality assurance in proton radiation therapy. Med Phys 2004;31:2107–2118. [PubMed: 15305464]
10. Jiang H, Paganetti H. Adaption of GEANT4 to Monte Carlo dose calculations based on CT data. Med Phys 2004;31:2811–2818. [PubMed: 15543788]
11. Schneider W, Bortfeld T, Schlegel W. Correlation between CT numbers and tissue parameters needed for Monte Carlo simulations of clinical dose distributions. Phys Med Biol 2000;45:459–478. [PubMed: 10701515]
12. Parodi K, Enghardt W, Haberer T. In-beam PET measurements of β^+-radioactivity induced by proton beams. Phys Med Biol 2002;47:21–36. [PubMed: 11814225]
13. Parodi K, Bortfeld T. A filtering approach based on Gaussian-powerlaw convolutions for local PET verification of proton radiotherapy. Phys Med Biol 2006;51:1991–2009. [PubMed: 16585841]
14. Tissue substitutes in radiation dosimetry and measurement. Bethesda: ICRU; 1989. ICRU Report 44
15. Tomitami T, Pawelke J, Kanazawa M, et al. Washout studies of ^{11}C in rabbit thigh muscle implanted by secondary beams of HIMAC. Phys Med Biol 2003;48:875–889. [PubMed: 12701892]
16. Mizuno H, Tomitami T, Kanazawa M, et al. Washout measurements of radioisotope implanted by radioactive beams in the rabbit. Phys Med Biol 2003;48:2269–2281. [PubMed: 12953897]
17. Conti M, Bendriem B, Casey M, et al. First experimental results of time-of-flight reconstruction on an LSO PET scanner. Phys Med Biol 2005;50:4507–4526. [PubMed: 16177486]

NIH-PA Author Manuscript

NIH-PA Author Manuscript

NIH-PA Author Manuscript

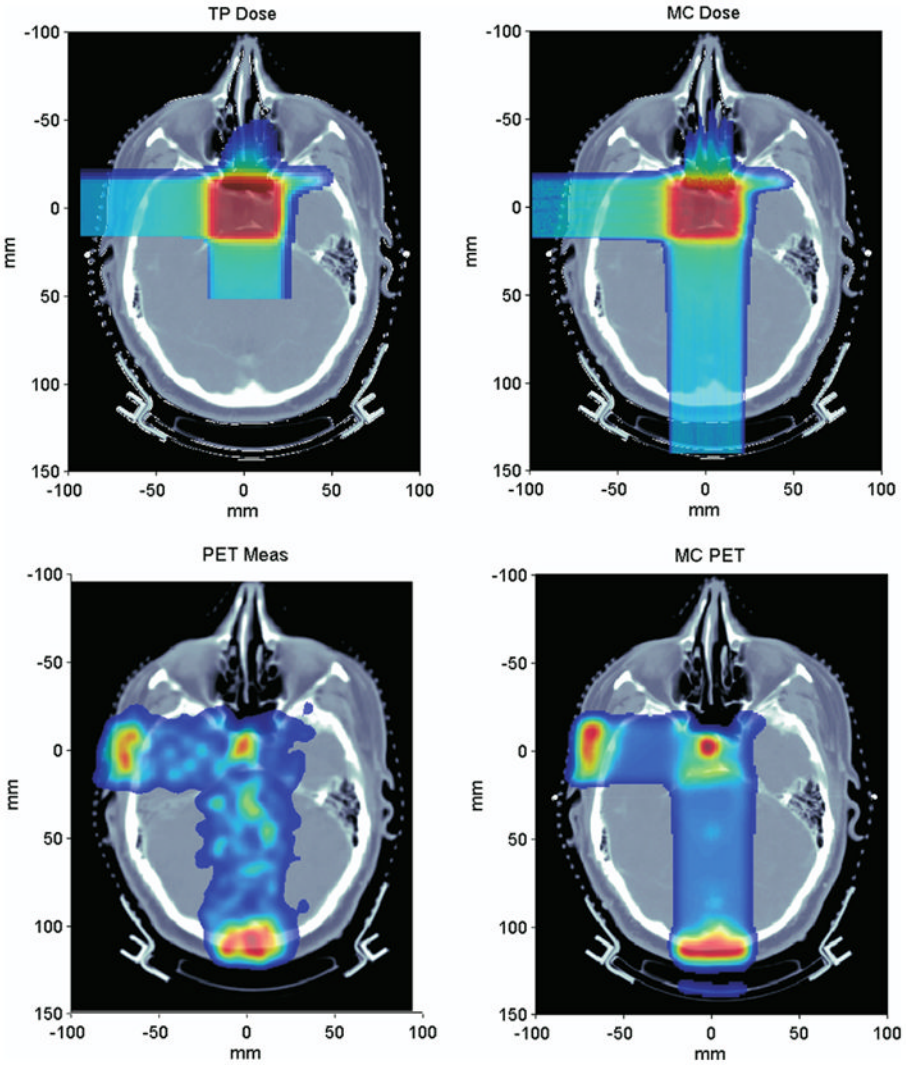

Fig 1.

Top: Treatment-plan (TP) (left) and Monte Carlo (MC)-recalculated (right) dose for a patient with pituitary adenoma receiving two orthogonal fields (lateral followed by posterior–anterior) at 0.9 GyE/field. Bottom: Measured (Meas) (left) and Monte Carlo-calculated (right) PET image. Delay times ΔT_1 and ΔT_2 to beginning of imaging were about 26 and 18 min from the end of the first and second field applications, respectively. Range of color wash display is from blue (minimum) to red (maximum).

NIH-PA Author Manuscript

NIH-PA Author Manuscript

NIH-PA Author Manuscript

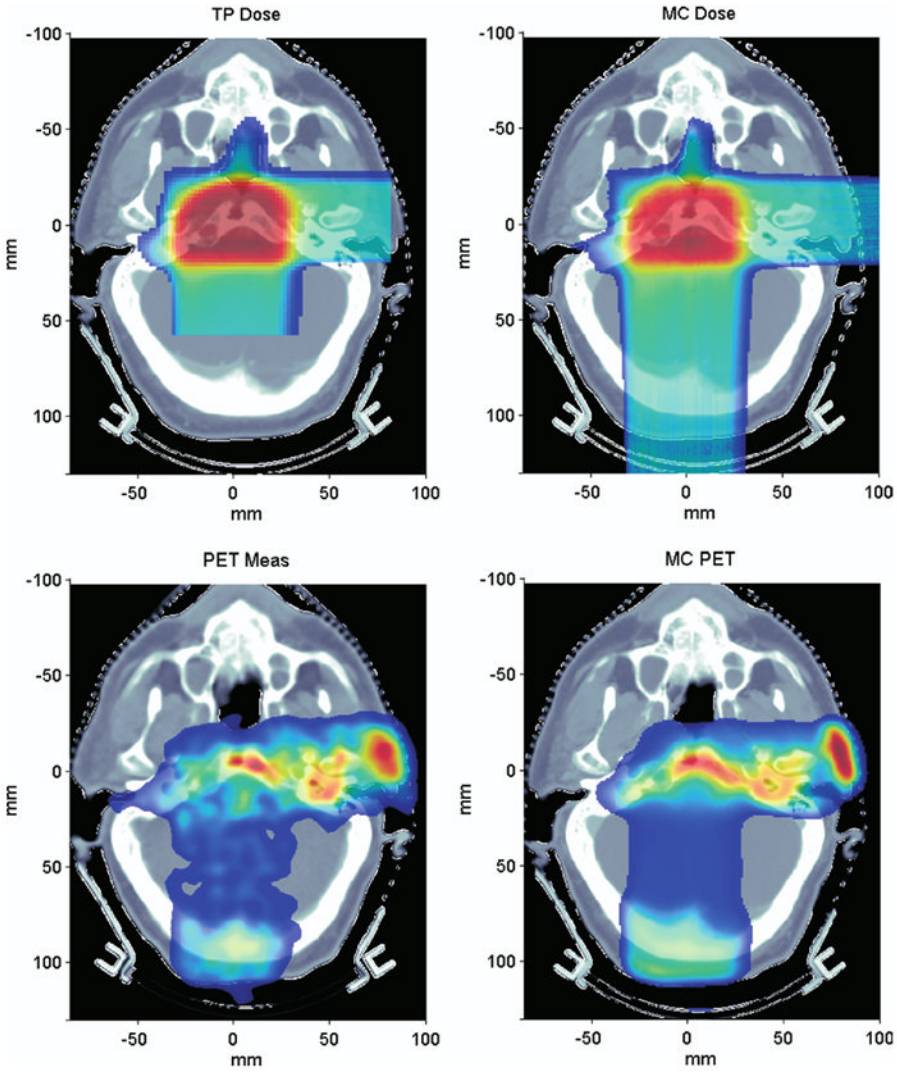

Fig 2.

As in Fig. 1, data for a patient with clival chordoma receiving a posterior–anterior followed by a lateral field (0.96 GyE each), imaged about 26 min (ΔT_1) and 16 min (ΔT_2) after completion. Range of color wash display is from blue (minimum) to red (maximum).

NIH-PA Author Manuscript

NIH-PA Author Manuscript

NIH-PA Author Manuscript

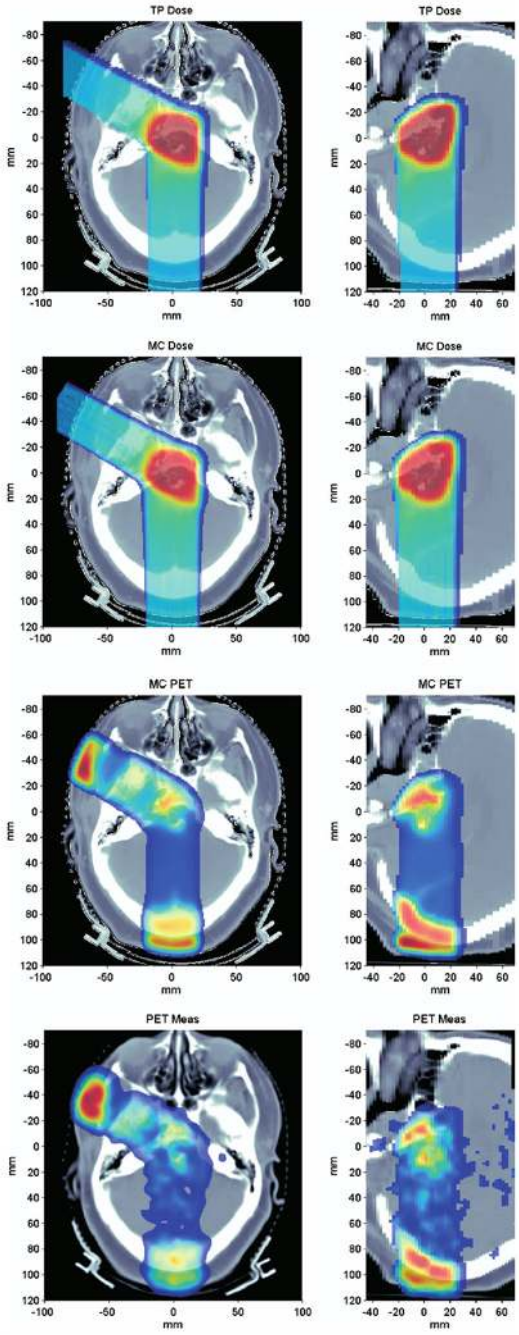

Fig 3.

Axial (left) and sagittal (right, lateral cut at 0 mm) views for a patient with clival chordoma receiving posterior–anterior followed by an oblique lateral field at 1 GyE/field, imaged with a delay of 20 min (ΔT_1) and 13 min (ΔT_2). Top to bottom: Treatment-planning (TP) and Monte Carlo (MC) dose, MC, and measured (Meas) positron emission tomography. Range of color wash display is from blue (minimum) to red (maximum).

NIH-PA Author Manuscript

NIH-PA Author Manuscript

NIH-PA Author Manuscript

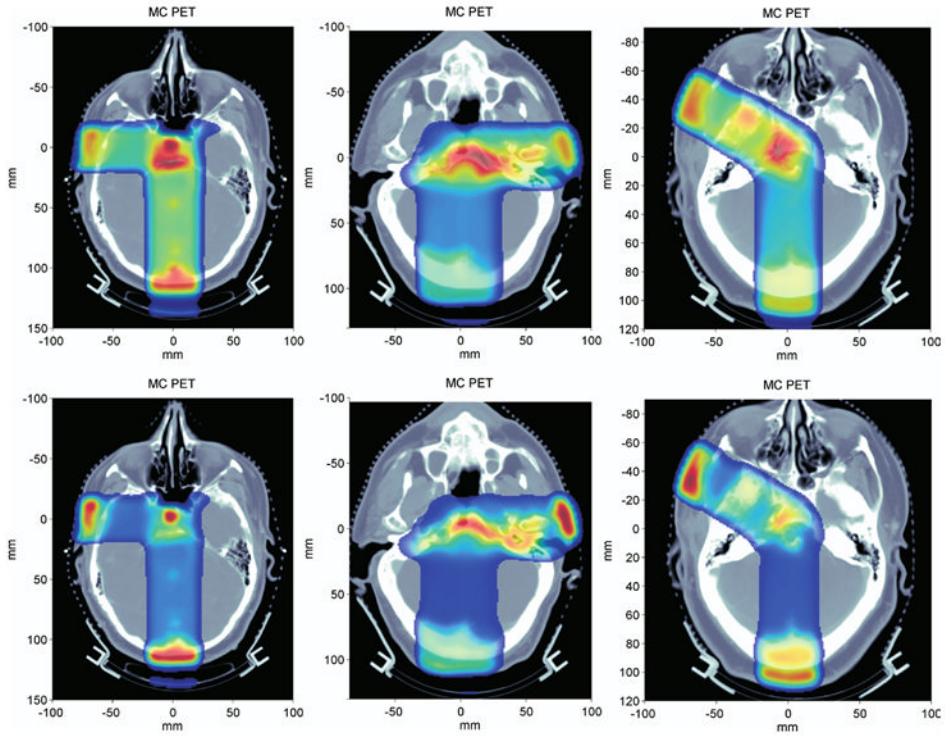

Fig 4.

Monte Carlo (MC) positron emission tomography (PET) calculations without (upper row) and with (bottom row) biologic decay correction for data of the same patient in Figs. 1 (left), 2 (middle), and 3 (right). Range of color wash display is from blue (minimum) to red (maximum).

NIH-PA Author Manuscript
NIH-PA Author Manuscript
NIH-PA Author Manuscript

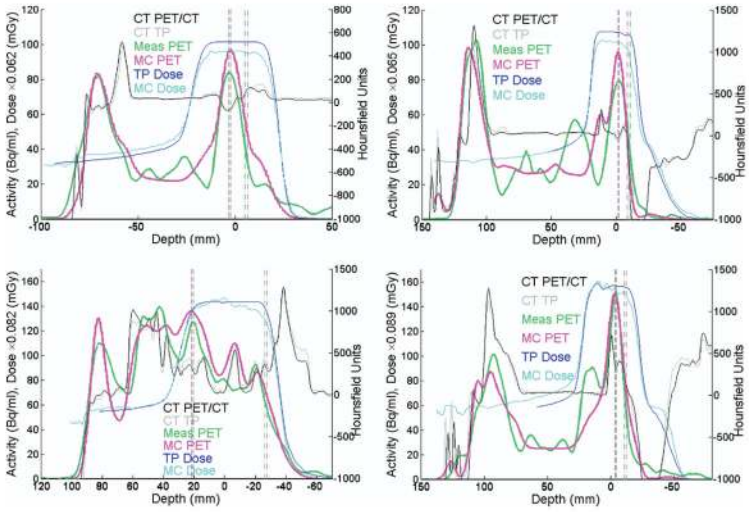

Fig 5.

Measured (Meas; green) and calculated (magenta) activity depth profiles for the lateral (left) and posterior–anterior (right) fields of Figs. 1 (top row) and 2 (bottom row), taken along the center and at 5 mm offset, respectively. Dashed and dashed-dotted lines mark the positions of the distal maximum and 50% fall-off, respectively. Planned (blue) and MC (blue) dose, as well as coregistered planning (TP; gray) and PET/CT (black) CT data, are shown.

NIH-PA Author Manuscript

NIH-PA Author Manuscript

NIH-PA Author Manuscript

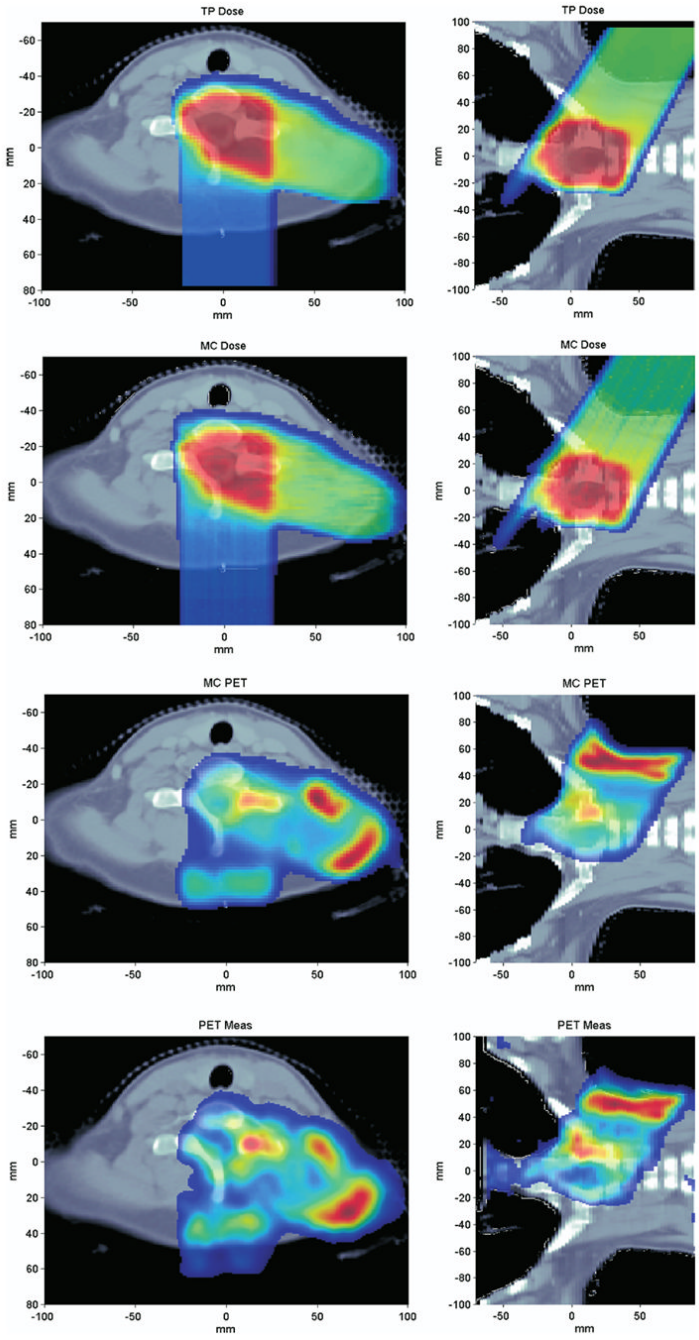

Fig 6.

Axial (left, as in Fig. 3) and coronal (right, cut at −10 mm) views for a T-spine chondrosarcoma patient receiving a 0.6-GyE posterior–anterior followed by a 1.2-GyE oblique superior–inferior field, imaged with a delay of 22 min (ΔT_1) and 16 min (ΔT_2). TP, treatment plan; MC, Monte Carlo. Range of color wash display is from blue (minimum) to red (maximum).

NIH-PA Author Manuscript
NIH-PA Author Manuscript
NIH-PA Author Manuscript

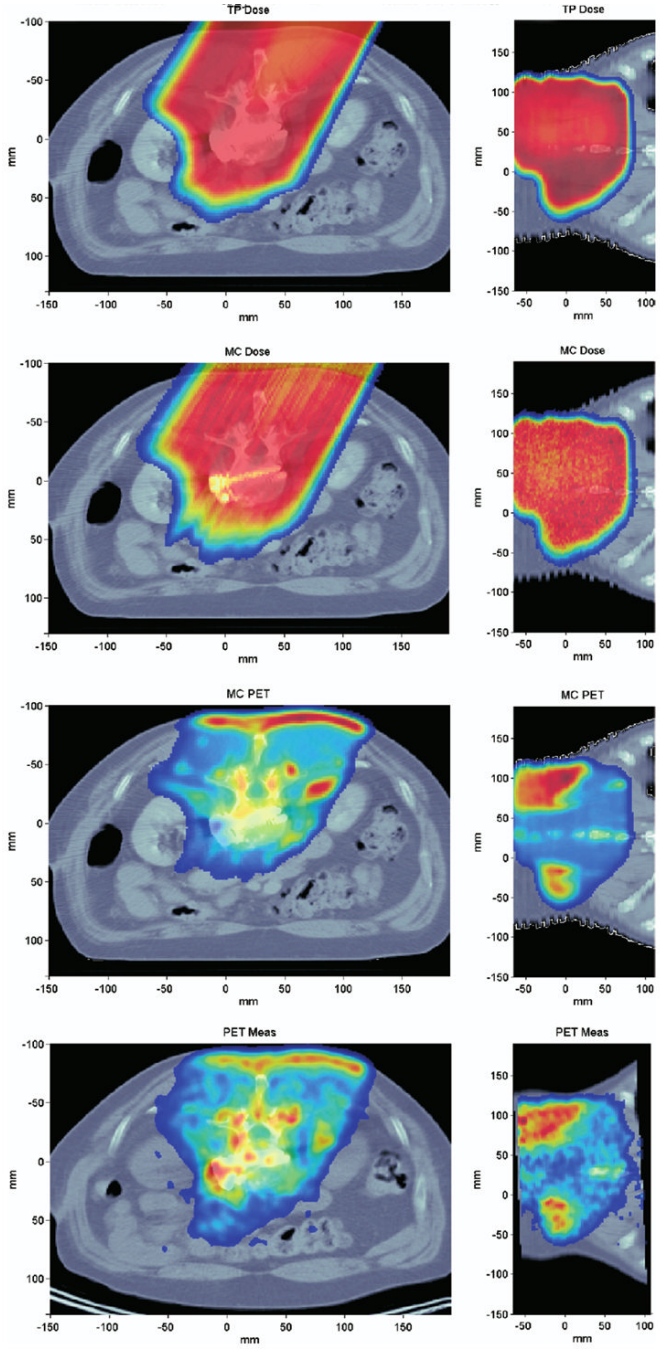

Fig 7.

Axial (left, as in Fig. 3) and coronal (right, cut at −70 mm) views for a L-spine chordoma patient receiving a 2-GyE oblique field imaged after $\Delta T \approx 17$ min. TP, treatment plan; MC, Monte Carlo. Range of color wash display is from blue (minimum) to red (maximum).

NIH-PA Author Manuscript

NIH-PA Author Manuscript

NIH-PA Author Manuscript

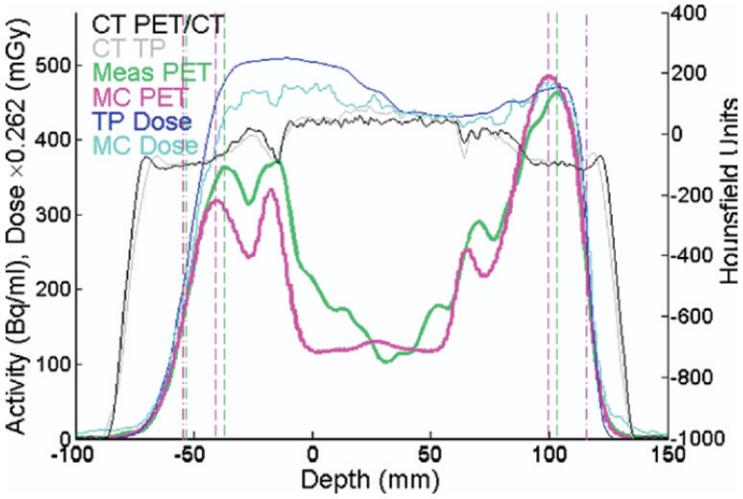

Fig 8.

Lateral profiles of coronal data shown in Fig. 7, taken at an axial position (horizontal axis) of 0 mm (compare Fig. 5 for color and line style legend). Meas = measured; TP = treatment plan; MC = Monte Carlo; CT = computed tomography; PET = positron emission tomography; Bq = Becquerel.

NIH-PA Author Manuscript

NIH-PA Author Manuscript

NIH-PA Author Manuscript

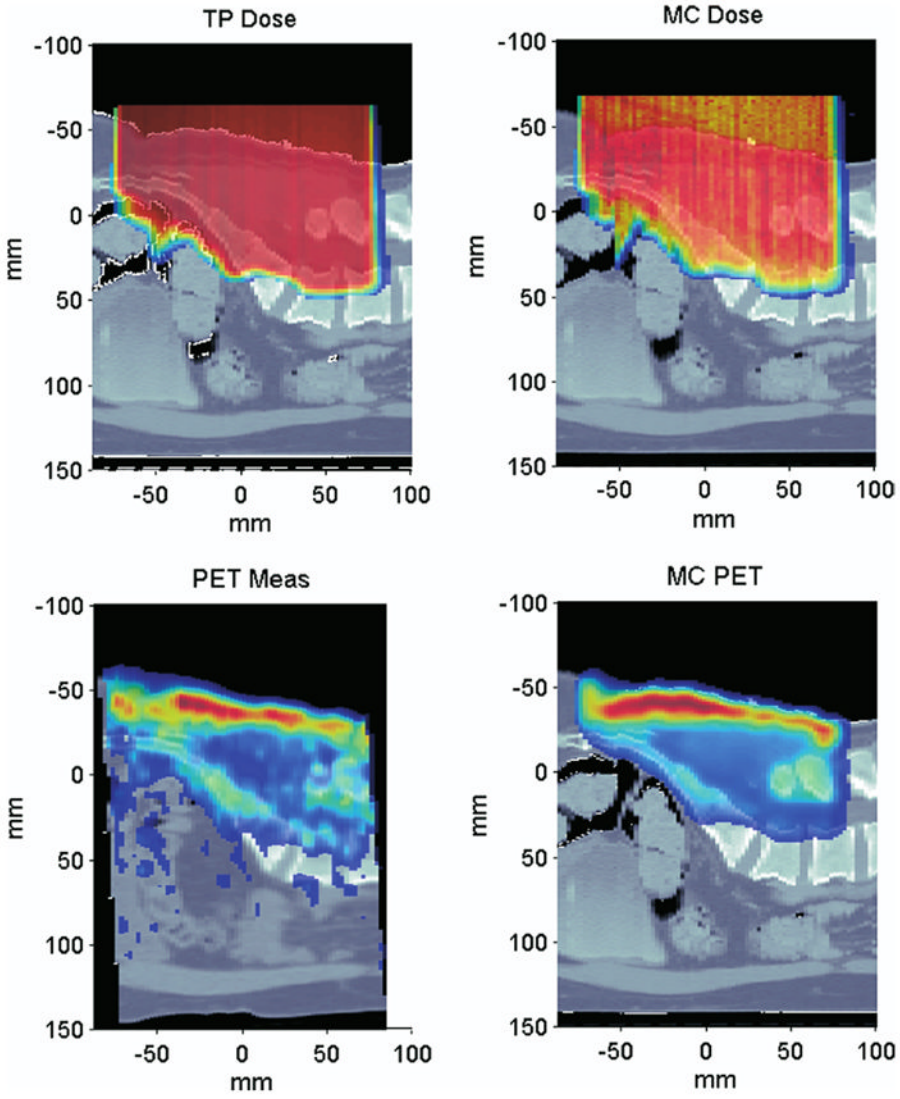

Fig 9.

Sagittal views for a sacral spindel cell sarcoma patient receiving a posterior-anterior field at 2 GyE, imaged about 16 min after treatment. Meas = measured; TP = treatment plan; MC = Monte Carlo. Range of color wash display is from blue (minimum) to red (maximum).

NIH-PA Author Manuscript
NIH-PA Author Manuscript
NIH-PA Author Manuscript

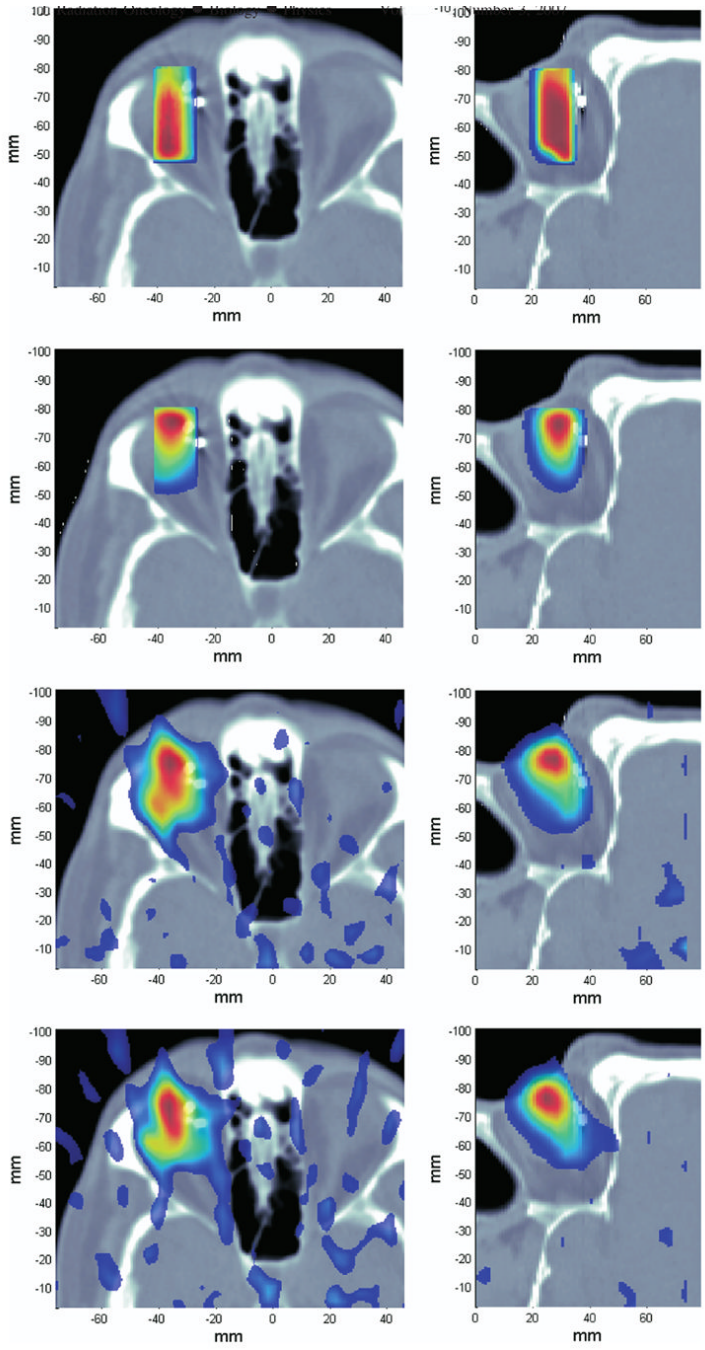

Fig 10.

Axial (left) and sagittal (right, cut at −30 mm) views of planned dose (top row) and calculated positron emission tomography (second row) against measurement (FBP; third row, all data; bottom row, first 10 min) for a patient with ocular melanoma receiving 10 GyE, imaged after $\Delta T \approx 19$ min. Treatment gazing angle was 26° polar, with no azimuthal rotation (*i.e.*, patient looking down). Range of color wash display is from blue (minimum) to red (maximum).

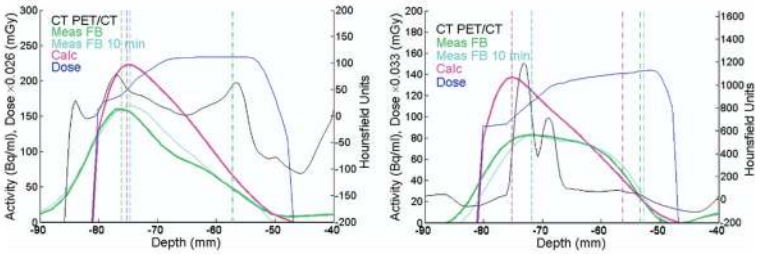

Fig 11.

Measured (Meas, FBP; green, all; blue, with *e.g.*, first 10 min; corrected in intensity for the shorter frame duration) and calculated (magenta) activity, as well as dose (blue) and CT (black) depth profiles, for a lateral (compare horizontal axis in Fig. 10, left) position of −30 mm at an axial cut of 30 mm (left) and 35 mm (right). Dashed and dashed-dotted lines mark maximum and 30% fall-off positions, respectively. Erroneous calculated intensity in the clips region (right) is due to incorrect composition assignment (cf. text). CT = computed tomography; FBP = filtered back projection; Bq = Becquerel; PET = positron emission tomography.

NIH-PA Author Manuscript
NIH-PA Author Manuscript
NIH-PA Author Manuscript

NIH-PA Author Manuscript

NIH-PA Author Manuscript

NIH-PA Author Manuscript

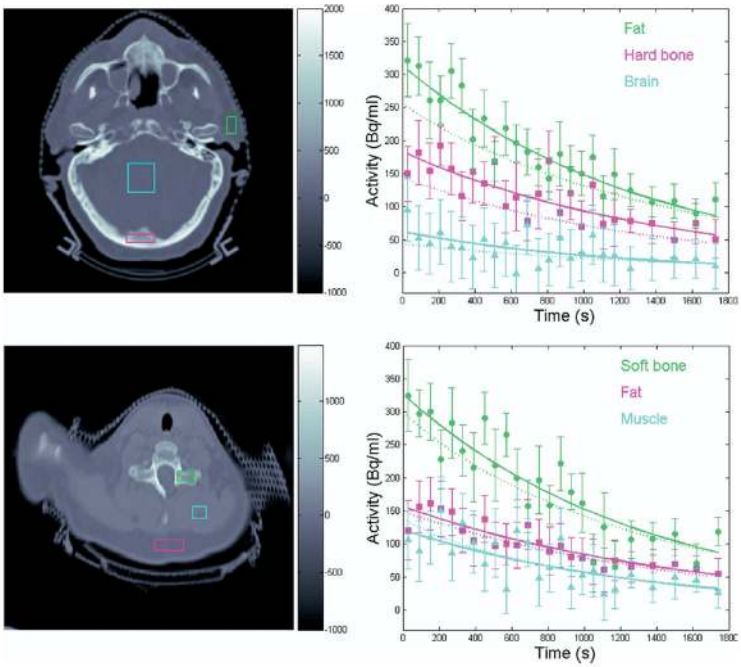

Fig 12.

Left: Regions of interest set in different tissues, marked in different colors in the PET/CT for a cranial base (top; compare Fig. 2) and a spine (bottom; compare Fig. 6). Right: Corresponding measured (symbols), fitted (solid line), and simulated (dotted line) activity decay curves for different tissue. CT = computed tomography; Bq = Becquerel; PET = positron emission tomography. The colors in the right panel refer to data taken in the anatomical region marked in the left panel with colored boxes. Measured data are shown as symbols (filled squares; circles; and triangles), fit to the measured data shown by solid lines, simu decays, are shown by dotted lines.

NIH-PA Author Manuscript
NIH-PA Author Manuscript
NIH-PA Author Manuscript

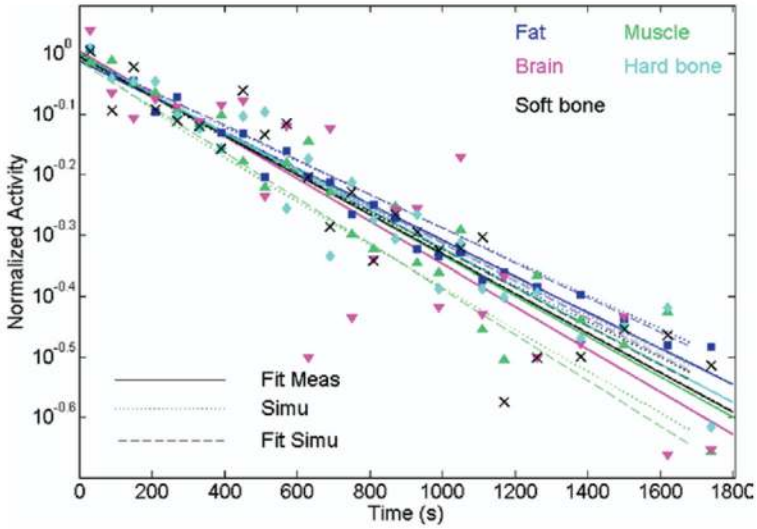

Fig 13.

Measured (Meas, symbols; compare errors in text) and simulated (Simu, dotted lines) activity decay curves averaged over more patient data for different tissues. Corresponding fits are shown by solid and dashed lines, respectively.

NIH-PA Author Manuscript NIH-PA Author Manuscript NIH-PA Author Manuscript

Table 1

Measured and Monte Carlo-calculated (in parentheses) distal-activity maximum, with its location (PET Max_{pos}) and the location of the 50% distal fall-off in comparison to the treatment plan and Monte Carlo (in parentheses) dose maximum, with corresponding 80% and 50% fall-off positions for the lateral and osterior–anterior fields of Fig. 5

Field	PET maximum (Bq/ml)	PET Max_{pos} (mm)	PET 50% (mm)	Dose maximum (Gy)	Dose 80% (mm)	Dose 50% (mm)
RL 1	84 (97)	−3.1 (−2.5)	5.1 (6.5)	1.64 (1.56)	19.5 (19.2)	22.6 (22.8)
PA 1	80 (96)	−2.3 (−1.7)	−10.8 (−8.9)	1.65 (1.57)	−15.9 (−12.9)	−20.8 (−18.7)
LR 2	127 (136)	20.5 (21.5)	−26.0 (−27.5)	1.75 (1.79)	−31.4 (−29.6)	−35.8 (−35.3)
PA 2	153 (151)	−4.5 (−3.5)	−10.7 (−12.3)	1.79 (1.81)	−20.9 (−19.2)	−25.9 (−25.0)

Abbreviations: RL/LR = lateral; PA = posterior–anterior; 1 = Fig. 5, top; 2 = Fig. 5, bottom; Bq = Becquerel.

NIH-PA Author Manuscript NIH-PA Author Manuscript NIH-PA Author Manuscript

Table 2

Fitted effective half-lives for measured and simulated decay curves averaged over more patient data for similar tissues of given average HU values

Tissue	HU	σ_{HU}	Measured $T_{eff,1/2}$ (s)	Relative error (%)	Simulated $T_{eff,1/2}$ (s)	Relative error (%)
Fat	−66	15	1,016	6	1,061	1
Muscle	44	7	904	11	802	2
Brain	33	4	858	22	979	1
Soft bone	346	111	925	15	954	2
Compact bone	1,195	195	948	12	982	1

Abbreviation: $T_{eff,1/2}$ = effective half-life.

Int J Radiat Oncol Biol Phys. Author manuscript; available in PMC 2007 October 31.